Mon. Not. R. Astron. Soc. **379,** 909–914 (2007) doi:10.1111/j.1365-2966.2007.11949.x

The supermassive black hole in NGC 4486a detected with SINFONI at the Very Large Telescope⋆

N. Nowak,[1]† R. P. Saglia,[1] J. Thomas,[2] R. Bender,[1,2] M. Pannella,[1] K. Gebhardt[3] and R. I. Davies[1]

[1]*Max-Planck-Institut für extraterrestrische Physik, Giessenbachstrasse, 85741 Garching, Germany*
[2]*Universitätssternwarte, Scheinerstrasse 1, 81679 Munich, Germany*
[3]*Astronomy Department, University of Texas, Austin, TX 78723, USA*

Accepted 2007 May 7. Received 2007 April 30; in original form 2007 January 8

ABSTRACT

The near-infrared (IR) integral field spectrograph SINFONI at the European Southern Observatory Very Large Telescope opens a new window for the study of central supermassive black holes. With a near-IR spatial resolution similar to *Hubble Space Telescope* optical and the ability to penetrate dust, it provides the possibility to explore the low-mass end of the $M_\bullet$–σ relation ($\sigma < 120\,\mathrm{km\,s^{-1}}$) where so far very few black hole masses were measured with stellar dynamics. With SINFONI, we observed the central region of the low-luminosity elliptical galaxy NGC 4486a at a spatial resolution of ≈0.1 arcsec in the *K* band. The stellar kinematics were measured with a maximum penalized likelihood method considering the region around the CO absorption band heads. We determined a black hole mass of $M_\bullet = (1.25^{+0.75}_{-0.79}) \times 10^7\,\mathrm{M}_\odot$ (90 per cent confidence limit) using the Schwarzschild orbit superposition method including the full two-dimensional spatial information. This mass agrees with the predictions of the $M_\bullet$–σ relation, strengthening its validity at the lower σ end.

Key words: galaxies: kinematics and dynamics – galaxies: individual: NGC 4486a.

1 INTRODUCTION

Studies of the dynamics of stars and gas in the nuclei of nearby galaxies during the last few years have established that all galaxies with a massive bulge component contain a central supermassive black hole (SMBH; Richstone et al. 1998; Bender & Kormendy 2003). Masses of these SMBHs ($M_\bullet$) are well correlated with the bulge luminosity or mass, respectively, and with the bulge velocity dispersion σ (Kormendy & Richstone 1995; Ferrarese & Merritt 2000; Gebhardt et al. 2000b). There are, however, still a lot of open questions in conjunction with the $M_\bullet$–σ correlation, among them are the exact slope, its universality and the underlying physics. A more precise knowledge of the behaviour of the $M_\bullet$–σ relation would help to constrain theoretical models of bulge formation and black hole growth (e.g. Silk & Rees 1998; Haehnelt & Kauffmann 2000; Burkert & Silk 2001, and others).

In inactive galaxies, the evidence for the existence of black holes and their masses comes from gravitational effects on the dynamics of stars inside the black hole's sphere of influence. Since the radius of the sphere of influence scales with the black hole mass $M_\bullet$, high-resolution observations are needed to detect SMBHs in the low-mass regime, even for the most nearby galaxies. Further difficulties arise from the presence of dust in many of these galaxies, particularly in discs, which enforces observations in the infrared (IR). Up to now, the low-mass regime ($\sigma \lesssim 120\,\mathrm{km\,s^{-1}}$) is sparsely sampled with only three dynamical black hole mass measurements (Milky Way, Schödel et al. 2002; M32, Verolme et al. 2002; NGC 7457, Gebhardt et al. 2003) and some upper limits (e.g. Gebhardt et al. 2001; Valluri et al. 2005). Since the near-IR integral-field spectrograph SINFONI became operational (Eisenhauer et al. 2003a; Bonnet et al. 2004), it is now possible to detect low-mass black holes in dust-obscured galaxies at a spatial resolution close to that of the *Hubble Space Telescope* (*HST*).

NGC 4486a is a low-luminosity elliptical galaxy in the Virgo cluster, close to M87. It contains an almost edge-on nuclear disc of stars and dust (Kormendy et al. 2005). The bright star ∼2.5 arcsec away from the centre makes it impossible to obtain undisturbed spectra with conventional ground-based longslit spectroscopy. However, it is one of the extremely rare cases, where an inactive, low-luminosity galaxy can be observed at diffraction limited resolution using adaptive optics with a natural guide star (NGS). This feature made NGC 4486a one of the most attractive targets during the years between the commissioning of SINFONI and similar instruments

⋆Based on observations at the European Southern Observatory (ESO) Very Large Telescope (VLT) (075.B-0236) and on observations made with the Advanced Camera for Surveys onboard the NASA/ESA *Hubble Space Telescope* (GO Proposals 9401, obtained from the ESO/ST-ECF Science Archive Facility)

†E-mail: nnowak@mpe.mpg.de

and the installation of laser guide stars (LGS). NGC 4486a is the first of our sample of galaxies observed or planned to be observed using near-IR integral-field spectroscopy with the goal to tighten the slope of the $M_\bullet$–σ relation in the low-σ regime ($\lesssim$120 km s^{-1}) and for pseudo-bulge galaxies.

This paper is structured as follows. In Section 2, we present the observations and the data reduction. The derivation of the kinematics and the photometry is described in Sections 3 and 4 and the dynamical modelling procedure is explained in Section 5. In Section 6, the results are presented and discussed and conclusions are drawn.

2 OBSERVATIONS AND DATA REDUCTION

NGC 4486a was observed on 2005 April 5 and 6, as part of guaranteed time observations with SINFONI (Eisenhauer et al. 2003a; Bonnet et al. 2004) at the Very Large Telescope (VLT) UT4. SINFONI consists of the integral-field spectrograph for IR faint field imaging (SPIFFI) (Eisenhauer et al. 2003b) and the Multi-Application Curvature Adaptive Optics (MACAO) module (Bonnet et al. 2003). We used the K-band grating (1.95–2.45 μm) and the 3×3 arcsec^2 field-of-view (0.05×0.1 arcsec^2 pixel^{-1}). The bright ($R \approx 11$ mag) star located ∼2.5 arcsec southwest of the nucleus was used for the AO correction. The seeing indicated by the optical seeing monitor was between 0.6 and 0.85 arcsec, resulting in a near-IR seeing better than ∼0.7 arcsec, which could be improved by the AO module to reach a resolution of 0.1 arcsec (∼25 per cent Strehl). For the chosen configuration, SINFONI delivers a nominal full width at half-maximum (FWHM) spectral resolution of $R \approx 4400$. In total, 14 on-source and seven sky exposures of 600 s each were taken in series of 'object–sky–object' cycles, dithered by up to 0.2 arcsec. During the last observation block, the visual seeing suddenly increased above 1.0 arcsec. Therefore, to keep the spatial resolution as high as possible only exposures with a seeing $\lesssim$ 0.85 arcsec were considered for the derivation of the kinematics. In order to derive the point spread function (PSF), an exposure of the AO star was taken regularly.

The SINFONI data reduction package SPRED (Schreiber et al. 2004; Abuter et al. 2006) was used to reduce the data. It includes all common reduction steps necessary for near-IR data plus routines to reconstruct the three-dimensional data cubes. After subtracting the sky frames from the object frames, the data were flat-fielded, corrected for bad pixels, for distortion and wavelength calibrated using a Ne/Ar lamp frame. The wavelength calibration was corrected using night-sky lines if necessary. Then, the three-dimensional data cubes were reconstructed and corrected for atmospheric absorption using the B9.5V star Hip 059503. As a final step, all data cubes were averaged together to produce the final data cube. Fig. 1 shows the resulting SINFONI image (collapsed cube) of NGC 4486a. The data of the telluric and the PSF stars were reduced likewise.

As PSF, we take the combined and normalized image of the PSF star exposures (see Fig. 2). Its core can be reasonably well fitted by a Gaussian profile with a FWHM of ∼100 mas (7.7 pc). The diameter of the sphere of influence of the black hole can be roughly estimated to 130 mas using the $M_\bullet$–σ relation of Tremaine et al. (2002), and is therefore resolved.

3 KINEMATICS

The kinematic information was extracted using the maximum penalized likelihood (MPL) technique of Gebhardt et al. (2000a), which obtains non-parametric line-of-sight velocity distributions

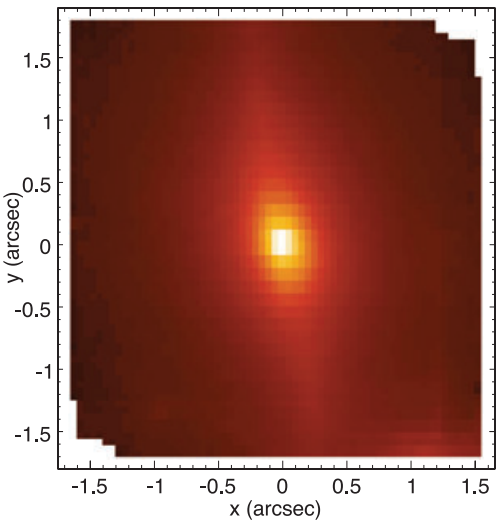

Figure 1. SINFONI image of NGC 4486a.

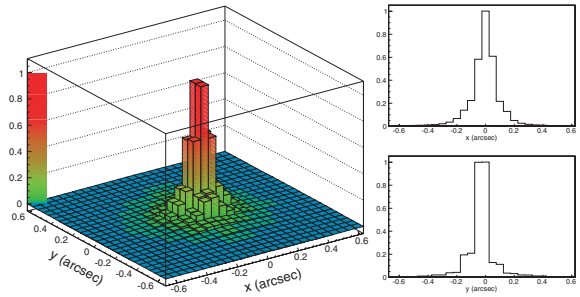

Figure 2. Left-hand panel: the two-dimensional PSF. Right-hand panel: x- and y-profiles of the PSF.

(LOSVDs). As kinematic template stars, we use six K0 to M0 stars which were observed during commissioning and our guaranteed time observations in 2005 with SINFONI using the same configuration as for NGC 4486a. Both galaxy and template spectra were continuum normalized. An initial binned velocity profile is convolved with a linear combination of the template spectra, and the residuals of the resulting spectrum to the observed galaxy spectrum are calculated. The velocity profile is then changed successively and the weights of the templates are adjusted in order to optimize the fit to the observed spectrum by minimizing the function $\chi^2_{\rm p} = \chi^2 + \alpha\mathcal{P}$, where α is the smoothing parameter that determines the level of regularization, and the penalty function $\mathcal{P}$ is the integral of the square of the second derivative of the LOSVD. We fitted only the first two band heads CO2–0 and CO3–1. The higher-order band heads are strongly disturbed by residual atmospheric features. At wavelength $\lambda < 2.29$ μm, the absorption lines are weak and cannot be fitted very well by the templates.

The uncertainties on the velocity profiles were estimated using Monte Carlo simulations (Gebhardt et al. 2000a). A galaxy spectrum is created by convolving the template spectrum with the measured LOSVD. Then, 100 realizations of that initial galaxy spectrum are created by adding appropriate Gaussian noise. The LOSVDs of each realization are determined and used to specify the confidence intervals.

In order to test the performance of the method on our SINFONI data and to find the best-fitting parameters, we performed Monte

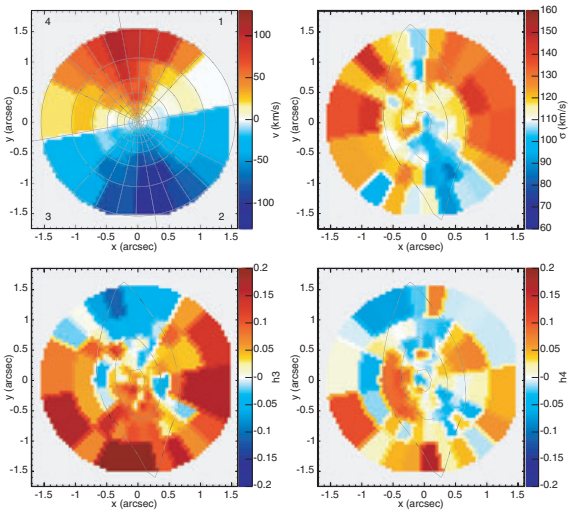

Figure 3. Stellar kinematic fields (v, σ, h_3, h_4) of NGC 4486a. The binning scheme and the numbering of the quadrants are overlaid over the velocity map and the isophotes are overlaid over the other maps for comparison.

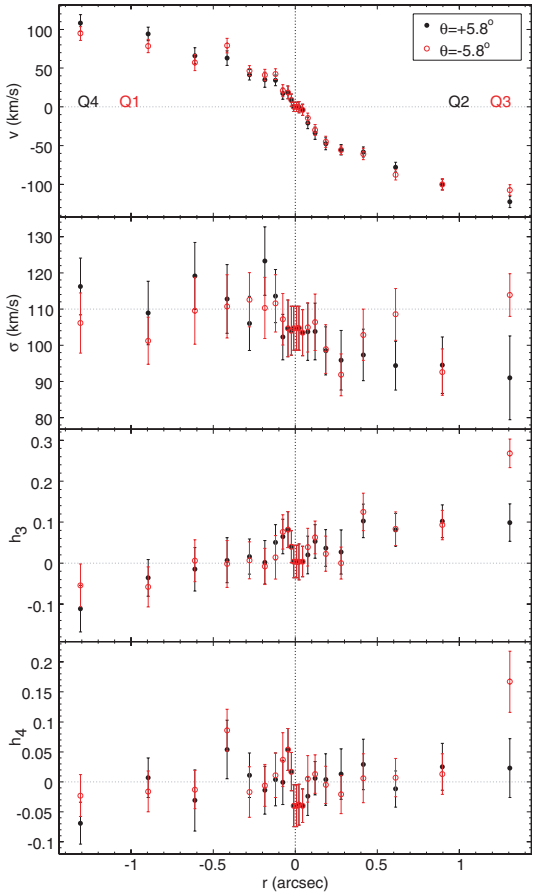

Figure 4. Stellar kinematic profiles (v, σ, h_3, h_4) of NGC 4486a along $\theta = \pm 5\overset{\circ}{.}8$ of the major axis. The corresponding quadrants crossed by the profiles are marked for easy identification in Fig. 3.

Carlo simulations on a large set of model galaxy spectra. These were created from stellar template spectra by convolving them with both Gaussian and non-Gaussian LOSVDs and by adding different amounts of noise. We found that the reconstructed LOSVDs resemble the input LOSVDs very well if the smoothing parameter α is chosen adequately (Merritt 1997; Joseph et al. 2001). The best choice of α solely depends on the signal-to-noise ratio (S/N) of the data. To maximize the S/N of the data, a binning scheme with 11 radial and five angular bins per quadrant, similar to that used in Gebhardt et al. (2003), was chosen. The centres of the angular bins are at latitudes $\theta = 5\overset{\circ}{.}8$, $17\overset{\circ}{.}6$, $30\overset{\circ}{.}2$, $45\overset{\circ}{.}0$ and $71\overset{\circ}{.}6$ from the major axis to the minor axis. The bins are not overlapping, but spatial resolution elements at the border between bins may be divided into parts where each part is counted to a different bin. The spectra within each bin were averaged with weights according to their share in the bin. The radial binning scheme ensures that an adequate S/N level comparable to that of the central spectrum (S/N $\approx$ 40) is maintained at all radii at the cost of spatial resolution outside the central region.

The resulting two-dimensional kinematics (v, σ, h_3, h_4) are presented in Fig. 3. It illustrates the superposition of the kinematics of the two distinct components in NGC 4486a – the disc and the bulge. Whereas the velocity map shows a regular rotation pattern, the cold stellar disc can be clearly distinguished from the surrounding hotter bulge in the velocity dispersion map. The velocity dispersion of the disc is $\approx$20–30 km s^{-1} smaller than that of the bulge. Asymmetric and symmetric deviations from a Gaussian velocity profile are quantified by the higher-order Gauss–Hermite coefficients h_3 and h_4 (Gerhard 1993; van der Marel & Franx 1993). Fig. 4 shows the kinematic profiles of NGC 4486a along the major axis at angles $\theta = +5\overset{\circ}{.}8$ and $-5\overset{\circ}{.}8$. The $+5\overset{\circ}{.}8$-profile agrees very well with the adjacent $-5\overset{\circ}{.}8$-profile within the error bars. When comparing the profiles at negative radii with the profiles at positive radii slight asymmetries can be seen (especially in σ), but as the errors are relatively large, deviations from axisymmetry are small.

The star at 2.5 arcsec from the centre, which heavily dilutes optical spectra of NGC 4486a taken without AO, does not have any significant effect on the kinematics derived here. Quadrant two is affected most, as it is located in the direction of the star. The fraction of inshining light from the star is only about 13 per cent at 0.7 arcsec from the centre of the galaxy in the direction of the star (the outermost point covered by the exposures of the PSF star) due to the narrow PSF. In addition, the spectrum of the star shows neither the strong CO absorption nor other spectral features in that wavelength region.

4 IMAGING

To derive the black hole mass in NGC 4486a, it is essential to determine the gravitational potential made up by the stellar component by deprojecting the surface brightness distribution. As NGC 4486a consists both kinematically and photometrically of two components with possibly different mass-to-light ratios Υ, we deproject bulge and disc separately.

To decompose the two components, we considered the *HST* images in the broad-band *F850LP* filter, with two Advanced Camera for Surveys (ACS) Wide Field Channel pointings of 560 s exposure each. The two dithers have no shift in spatial coordinates. The data were reduced by the ST-ECF On-The-Fly Recalibration system (see http://archive.eso.org/archive/hst for detailed information).

Moreover, we use the GALFIT package (Peng et al. 2002) to fit PSF-convolved analytic profiles to the two-dimensional surface brightness of the galaxy. The code determines the best fit by comparing the convolved models with the science data using a Levenberg–Marquardt downhill gradient algorithm to minimize the χ^2 of the

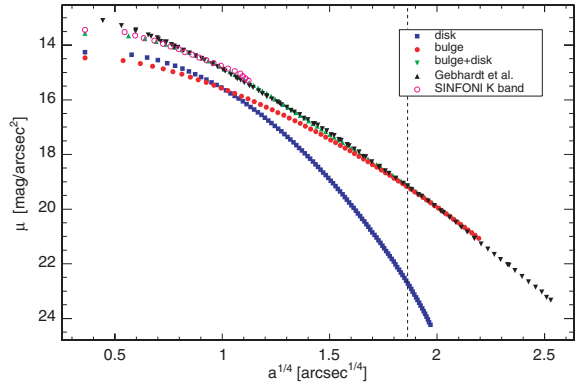

Figure 5. Surface brightness profile for NGC 4486a. At radii left of the dashed line, we used the decomposed bulge and disc profiles for the deprojection, right of the dashed line we used the profile of Gebhardt et al. (in preparation) (scaled to ACS z band).

fit. The saturated star close to the galaxy centre has been masked out from the modelling. The observing strategy, that is, the adopted no spatial shift between the two dithers, has allowed us to obtain a careful description of the PSF by using the TINYTIM[1] code.

We modelled the galaxy light with a double Sérsic (1968) model with indices $n = 2.19$ for the bulge and $n = 1.67$ for the disc. In Fig. 5, we show the surface brightness profiles of bulge, disc, bulge+disc, and for comparison the SINFONI surface brightness profile and the un-decomposed profile of Gebhardt et al. (in preparation), which was derived from *HST* and Canada–France–Hawaii Telescope imaging in several bands. This profile agrees very well with our combined profile and we use it, scaled to match our profile, at radii >11.5 arcsec where the bulge strongly dominates.

Bulge and disc were then deprojected separately using the program of Magorrian (1999) under the assumption that both components are edge-on and axisymmetric. The stellar mass density can then be modelled as in Davies et al. (2006) via $\rho_* = \Upsilon_{\rm bulge}\nu_{\rm bulge} + \Upsilon_{\rm disc}\nu_{\rm disc}$, where ν is the luminosity density obtained from the deprojection and the ACS z band mass-to-light ratio Υ is assumed to be constant with radius for both components.

5 SCHWARZSCHILD MODELLING

The mass of the black hole in NGC 4486a was determined based on the Schwarzschild (1979) orbit superposition technique, using the code of Gebhardt et al. (2000a, 2003) in the version of Thomas et al. (2004). It comprises the following usual steps. (1) Calculation of a potential with a trial black hole of mass $M_\bullet$ and a stellar mass density ρ_*. (2) A representative set of orbits is run in this potential and an orbit superposition that best matches the observational constraints is constructed. (3) Repetition of the first two steps with different values for $\Upsilon_{\rm bulge}$, $\Upsilon_{\rm disc}$ and $M_\bullet$ until the eligible parameter space is systematically sampled. The best-fitting parameters then follow from a χ^2 analysis.

The models are calculated on the grid with 11 radial and five angular bins per quadrant as described above (cf. Fig. 3).

Our orbit libraries contain 2×7000 orbits. The luminosity density is a boundary condition and hence exactly reproduced. The 11×5 LOSVDs are binned into 17 velocity bins each and then fitted directly, not the parametrized moments. We limit the parameter space for the values of Υ by considering the population synthesis model of Maraston (1998, 2005), which gives us $\Upsilon \lesssim 5$ for the z band.

Special care was taken when implementing the PSF. Due to its special shape with the narrow core and the broad wings (cf. Fig. 2), the PSF was not fitted, rather the two-dimensional image of the star was directly used for convolving our models.

6 RESULTS

A big advantage of integral-field data compared to longslit data is that we can check the assumption of axisymmetry by comparing the kinematics of the four quadrants and quantify the effect of possible deviations by modelling each quadrant separately. We do not find major differences in the kinematics of the four quadrants (cf. Figs 3 and 4). As it takes a large amount of computing time to calculate all models with different mass-to-light ratios for bulge and disc for each quadrant, we used the same Υ for bulge and disc for the comparison of the quadrants. In Table 1, the resulting values for $M_\bullet$ and Υ are listed. They show that the four quadrants agree reasonably well with each other. The only systematically deviant point is the $M_\bullet$ determination in the first quadrant that, however, has a large error and therefore is compatible within the 90 per cent confidence limit (CL) with the other three quadrants. Therefore, we symmetrized the LOSVDs by taking for each bin the weight-averaged LOSVDs of the four quadrants and the corresponding errors. The results of modelling these averaged LOSVDs are shown in Fig. 6, where $\Delta\chi^2_0 = \chi^2 - \chi^2_{\rm min}$ is plotted as a function of $(\Upsilon_{\rm bulge} + \Upsilon_{\rm disc})/2$ and $M_\bullet$ with error contours for two degrees of freedom. $\Upsilon_{\rm bulge}$ and $\Upsilon_{\rm disc}$ anticorrelate such that their sum is approximately constant, as shown in the upper part of Fig. 6. A black hole mass of $(1.25^{+0.75}_{-0.79}) \times 10^7\,{\rm M}_\odot$ (90 per cent CL) can be fitted with $\Upsilon_{\rm disc} \approx 2.8 \ldots 5.2$ and $\Upsilon_{\rm bulge} \approx 2.8 \ldots 4.8$. The result agrees within 90 per cent CL with the results of all quadrants shown in Table 1. The best-fitting model, obtained with minimal regularization, is marked with a white circle and has a black hole mass $M_\bullet = 1.25 \times 10^7\,{\rm M}_\odot$ and mass-to-light ratios $\Upsilon_{\rm disc} = 4.0$ and $\Upsilon_{\rm bulge} = 3.6$. The difference in χ^2 to the best-fitting model without black hole is 24.14 which corresponds to 4.5σ. The total χ^2 values for the models are around 300. Together with the number of observables (11 radial bins × five angular bins × 17 velocity bins), this gives a reduced χ^2 of ≈0.3. Note, however, that the number of observables is in reality smaller due to the smoothing (Gebhardt et al. 2000a).

The dynamical mass-to-light ratios of disc and bulge agree with an old and metal-rich stellar population (Maraston 1998, 2005). $\Upsilon_{\rm disc}$ tends to be larger than $\Upsilon_{\rm bulge}$ which is probably due to the presence of dust in the disc. To estimate the effect of the dust on the mass-to-light ratio of the disc, we are using the model of

Table 1. Results obtained for the four quadrants separately with a global mass-to-light ratio (90 per cent CL). The numbering of the quadrants can be inferred from Fig. 3.

Quadrant	$M_\bullet(10^7\,{\rm M}_\odot)$	Υ
1	$4.0^{+0.7}_{-2.4}$	$3.4^{+0.6}_{-0.6}$
2	$1.0^{+1.1}_{-0.2}$	$3.6^{+0.2}_{-0.5}$
3	$1.0^{+0.5}_{-0.5}$	$3.8^{+0.6}_{-0.1}$
4	$1.5^{+1.0}_{-1.0}$	$4.4^{+0.3}_{-0.9}$
1–4 averaged	$1.25^{+0.3}_{-0.3}$	$4.0^{+0.1}_{-0.4}$

[1] http://www.stsci.edu/software/tinytim/tinytim.

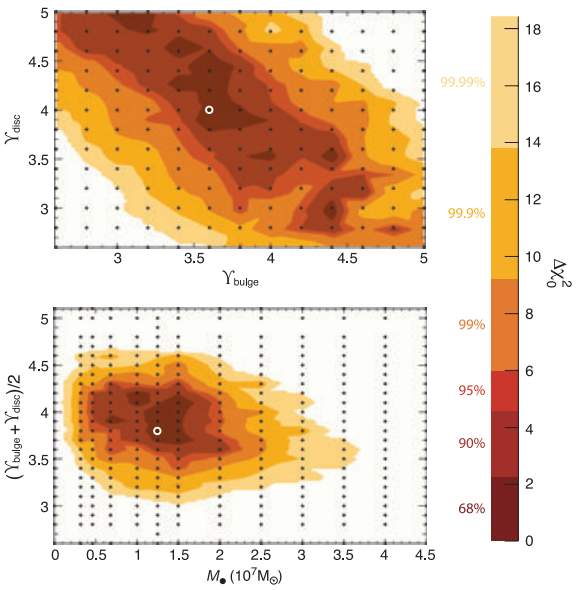

Figure 6. $\Delta\chi^2_0 = \chi^2 - \chi^2_{min}$ as a function of (top) Υ_{bulge} and Υ_{disc}, minimized over $M_\bullet$; (bottom) $M_\bullet$ and $(\Upsilon_{bulge} + \Upsilon_{disc})/2$. The black points are the models we calculated and the coloured regions are the (unsmoothed) confidence intervals for two degrees of freedom. The best-fitting model is marked with a white circle.

Pierini et al. (2004). For the *HST-F850LP* filter and an assumed typical optical depth $\tau \lesssim 0.5$, we obtain an attenuation of $A_\lambda \lesssim 0.36$ mag. This translates the best-fitting $\Upsilon_{disc} = 4.0$ to a significantly smaller dust-corrected value of $\gtrsim 2.9$. Following the models of Maraston (1998, 2005), this is in good agreement with an estimated $\gtrsim 2$ Gyr younger disc (Kormendy et al. 2005).

The significance of the result is illustrated in Fig. 7. It shows the χ^2 difference between the best-fitting model without black hole and the best-fitting model with black hole [$\Delta\chi^2 = \sum_{i=1}^{17} (\chi^2_{i,noBH} - \chi^2_{i,BH})$ over all 17 velocity bins] for all LOSVDs of the averaged quadrant. The part outside ≈2.5 spheres of influence, where the dynamical effect of the black hole is negligible, is displayed in a compressed way in order to emphasize the important inner part. For 75 per cent of all bins, the model with black hole produces a fit to the LOSVD better than the model without black hole. The signature of the black hole is imprinted mainly along the major axis, where the largest positive $\Delta\chi^2$ are found at radii $r \approx 0.09, \ldots, 0.22$ arcsec. At radii $r \lesssim 0.09$ arcsec, the differences between both models are smaller due to the effect of the PSF. For the radii with the largest $\Delta\chi^2$ along the major axis, the LOSVD and the fits with and without black hole are shown in the left-hand panels of Fig. 7, together with the corresponding $\Delta\chi^2_i$ as a function of the line-of-sight velocity. The differences between the two fits are relatively small in absolute terms. However, the model without black hole has more stars on the low-velocity wing at a $\sim 1.5\sigma$ level, failing to match fully the measured slightly higher mean velocity of the galaxy. Future observations with a higher spatial resolution should be able to probe this difference more clearly.

The total stellar mass within one sphere of influence, where the imprint of the black hole is strongest, is $M_* = 9.84 \times 10^6\,M_\odot$. If the additional mass of $M_\bullet = 1.25 \times 10^7\,M_\odot$ was solely composed of stars, this would increase the mass-to-light ratio to $\Upsilon_{disc} \approx 9.1$ (6.6 if we take into account the dust absorption), a region which is excluded by stellar population models or at least requires unrealistic high stellar ages.

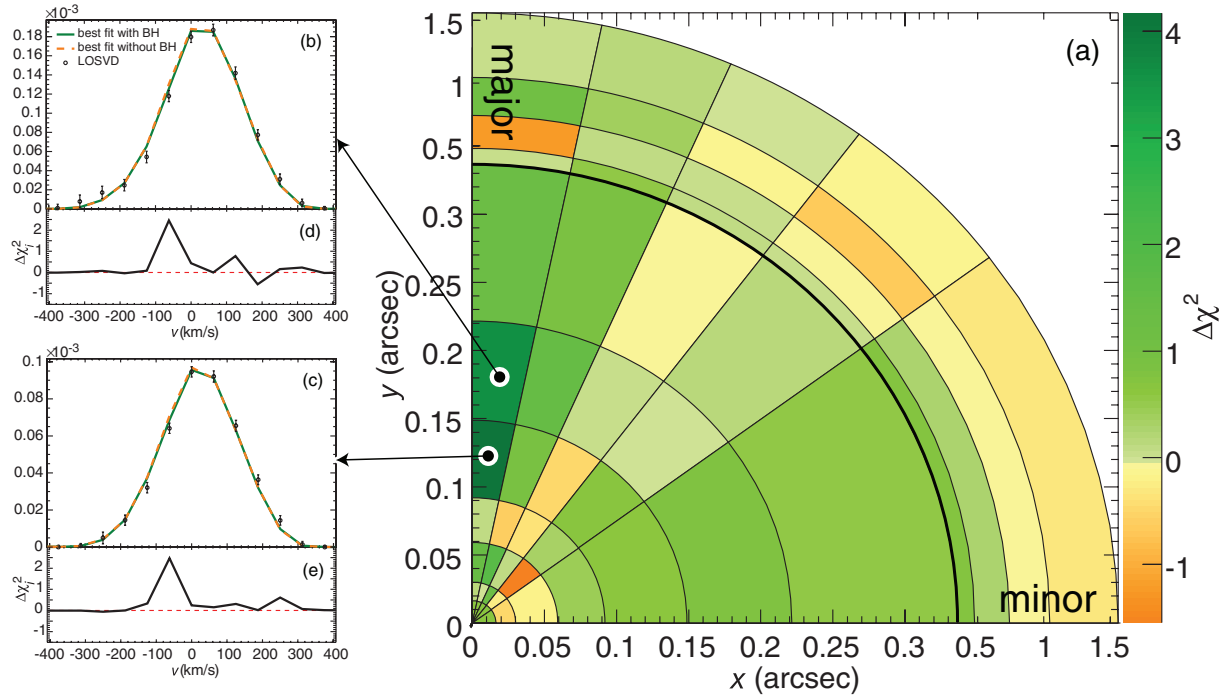

Figure 7. (a) χ^2 difference between the best-fitting model without black hole and the best-fitting model with black hole ($\Delta\chi^2 = \sum_i \Delta\chi^2_i = \sum_{i=1}^{17} (\chi^2_{i,noBH} - \chi^2_{i,BH})$ over all 17 velocity bins) for all LOSVDs of the averaged quadrant. Bins where the model with black hole fits the LOSVD better are plotted in green and the others in orange. The part outside ≈2.5 spheres of influence is plotted with a different scale than the inner part, since in the outer region the dynamical effect of the black hole (and therefore the difference between the two models) is negligible. (b and c) For the radii with the largest positive χ^2 difference in (a) the LOSVD (open circles with error bars, normalized as in Gebhardt et al. 2000a) and both fits (with black hole, full green line and without black hole, dashed orange line) are shown with the corresponding $\Delta\chi^2_i$ plotted below (d and e).

The models with black hole become tangentially anisotropic in the centre, while the models without black hole are close to isotropic.

Our result is in good agreement with the prediction of the $M_\bullet$–σ relation ($1.26^{+0.49}_{-0.35} \times 10^7\,\mathrm{M}_\odot$ using the result of Tremaine et al. 2002) and strengthens it in the low-σ regime ($\lesssim$120 km s^{-1}), where, besides several upper limits, up to now only three black hole masses were measured with stellar kinematics (Milky Way, Schödel et al. 2002; M32, Verolme et al. 2002; NGC 7457, Gebhardt et al. 2003).

NGC 4486a is only the first object in our sample of low-mass galaxies under investigation. The LGS, which was recently installed at the VLT UT4, makes observations of a large number of appropriate galaxies now possible. Therefore, we plan to further explore this region of the $M_\bullet$–σ relation by observing more galaxies with velocity dispersions between the resolution limit of SINFONI ($\sim$30 km s^{-1}) and $\sim$120 km s^{-1}.

ACKNOWLEDGMENTS

We are grateful to Frank Eisenhauer and Stefan Gillessen for assistance in using the SINFONI instrument and the reduction software SPRED. Furthermore, we thank David Fisher for providing us the surface brightness profile which we used at large radii.

REFERENCES

Abuter R., Schreiber J., Eisenhauer F., Ott T., Horrobin M., Gillessen S., 2006, New Astron. Rev., 50, 398
Bender R., Kormendy J., 2003, in Shaver P., Dilella L., Giménez A., eds, Astronomy, Cosmology and Fundamental Physics. Springer-Verlag, Berlin, p. 262
Bonnet H. et al., 2003, in Wizinowich P., Bonaccini D., eds, Proc. SPIE Vol. 4839, Adaptive Optical System Technologies II. SPIE, Bellingham WA, p. 329
Bonnet H. et al., 2004, ESO Messenger, 117, 17
Burkert A., Silk J., 2001, ApJ, 554, L151
Davies R. I. et al., 2006, ApJ, 646, 754
Eisenhauer F. et al., 2003a, in Iye M., Moorwood A., eds, Proc. SPIE Vol. 4841, SINFONI – Integral Field Spectroscopy at 50 Milliarcsecond Resolution with the ESO VLT. SPIE, Bellingham WA, p. 1548
Eisenhauer F. et al., 2003b, ESO Messenger, 113, 17
Ferrarese L., Merritt D., 2000, ApJ, 539, L9
Gebhardt K. et al., 2000a, AJ, 119, 1157
Gebhardt K. et al., 2000b, ApJ, 539, L13
Gebhardt K. et al., 2001, AJ, 122, 2469
Gebhardt K. et al., 2003, ApJ, 583, 92
Gerhard O., 1993, MNRAS, 265, 213
Haehnelt M. G., Kauffmann G., 2000, MNRAS, 318, L35
Joseph C. L. et al., 2001, ApJ, 550, 668
Kormendy J., Richstone D., 1995, ARA&A, 33, 581
Kormendy J., Gebhardt K., Fisher D., Drory N., Macchetto F. D., Sparks W., 2005, AJ, 129, 2636
Magorrian J., 1999, MNRAS, 302, 530
Maraston C., 1998, MNRAS, 300, 872
Maraston C., 2005, MNRAS, 362, 799
Merritt D., 1997, AJ, 114, 228
Peng C. Y., Ho L. C., Impey C. D., Rix H.-W., 2002, AJ, 124, 266
Pierini D., Gordon K. D., Witt A. N., Madsen G. J., 2004, ApJ, 617, 1022
Richstone D. et al., 1998, Nat, 395, A14
Schödel R. et al., 2002, Nat, 419, 694
Schreiber J., Thatte N., Eisenhauer F., Tecza M., Abuter R., Horrobin M., 2004, in Ochsenbein F., Allen M., Egret D., eds, ASP Conf. Proc. Vol. 314, Data Reduction Software for the VLT Integral Field Spectrometer SPIFFI. Astron. Soc. Pac., San Francisco, p. 380
Schwarzschild M., 1979, ApJ, 232, 236
Sérsic J. L., 1968, Atlas De Galaxias Australes. Observatorio Astronomico, Cordoba, Argentina
Silk J., Rees M. J., 1998, A&A, 331, 1
Thomas J., Saglia R., Bender R., Thomas D., Gebhardt K., Magorrian J., Richstone D., 2004, MNRAS, 353, 391
Tremaine S. et al., 2002, ApJ, 574, 740
Valluri M., Ferrarese L., Merritt D., Joseph C. L., 2005, ApJ, 628, 137
van der Marel R., Franx M., 1993, ApJ, 407, 525
Verolme E. K. et al., 2002, MNRAS, 335, 517

This paper has been typeset from a TEX/LATEX file prepared by the author.